


The MeerKAT Galaxy Cluster Legacy Survey

I. Survey Overview and Highlights[★]

K. Knowles^{1,2,3} , W. D. Cotton^{4,3}, L. Rudnick⁵, F. Camilo³, S. Goedhart³, R. Deane^{6,7}, M. Ramatsoku^{2,8}, M. F. Bietenholz^{9,10}, M. Brüggen¹¹, C. Button⁷, H. Chen¹², J. O. Chibueze^{13,14}, T. E. Clarke¹⁵, F. de Gasperin^{11,16}, R. Ianjamasimanana^{2,3}, G. I. G. Józsa^{3,2,17}, M. Hilton^{1,18}, K. C. Kesebonye^{1,18}, K. Kolokythas¹³, R. C. Kraan-Korteweg¹², G. Lawrie^{6,7}, M. Lochner^{19,3}, S. I. Loubser¹³, P. Marchegiani^{6,20}, N. Mhlahlo⁶, K. Moodley^{1,18}, E. Murphy⁴, B. Namumba², N. Oozeer^{3,21}, V. Parekh^{2,3}, D. S. Pillay^{1,18}, S. S. Passmoor³, A. J. T. Ramaila³, S. Ranchod^{6,7}, E. Retana-Montenegro^{1,18}, L. Sebokolodi², S. P. Sikhosana^{1,18}, O. Smirnov^{2,3}, K. Thorat^{7,22}, T. Venturi¹⁶, T. D. Abbott³, R. M. Adam³, G. Adams³, M. A. Aldera²³, E. F. Bauermeister³, T. G. H. Bennett³, W. A. Bode³, D. H. Botha²⁴, A. G. Botha³, L. R. S. Brederode^{3,25}, S. Buchner³, J. P. Burger³, T. Cheetham³, D. I. L. de Villiers²⁶, M. A. Dikgale-Mahlakoana³, L. J. du Toit²⁴, S. W. P. Esterhuysen³, G. Fadana³, B. L. Fanaroff³, S. Fataar³, A. R. Foley³, D. J. Fourie³, B. S. Frank^{3,22,12}, R. R. G. Gamatham³, T. G. Gatsi³, M. Geyer³, M. Gouws³, S. C. Gumede³, I. Heywood^{27,2,3}, M. J. Hlakola³, A. Hokwana³, S. W. Hoosen³, D. M. Horn³, J. M. G. Horrell^{3,28}, B. V. Hugo^{3,2}, A. R. Isaacson³, J. L. Jonas^{2,3}, J. D. B. Jordaan^{3,24}, A. F. Joubert³, R. P. M. Julie³, F. B. Kapp³, V. A. Kasper³, J. S. Kenyon^{2,3}, P. P. A. Kotzé³, A. G. Kotze³, N. Kriek³, H. Kriel³, V. K. Krishnan³, T. W. Kusel³, L. S. Legodi³, R. Lehmensiek^{24,26}, D. Liebenberg³, R. T. Lord³, B. M. Lunsy³, K. Madisa³, L. G. Magnus³, J. P. L. Main³, A. Makhaba³, S. Makhathini⁶, J. A. Malan³, J. R. Manley³, S. J. Marais²⁴, M. D. J. Maree³, A. Martens³, T. Mauch³, K. McAlpine³, B. C. Merry³, R. P. Millenaar³, O. J. Mokone³, T. E. Monama²⁹, M. C. Mphego³, W. S. New³, B. Ngcebetsha^{3,2}, K. J. Ngoasheng³, M. T. Ockards³, A. J. Otto^{3,25}, A. A. Patel³, A. Peens-Hough³, S. J. Perkins³, N. M. Ramanujam^{3,30}, Z. R. Ramudzuli³, S. M. Ratcliffe³, R. Renil³, A. Robyntjies³, A. N. Rust³, S. Salie³, N. Sambu³, C. T. G. Schollar³, L. C. Schwardt³, R. L. Schwartz³, M. Serylak^{25,3,19}, R. Siebrits³, S. K. Sirothia^{3,2}, M. Slabber³, L. Sofeya³, B. Taljaard³, C. Tasse^{31,2}, A. J. Tiplady³, O. Toruvanda³, S. N. Twum³, T. J. van Balla³, A. van der Byl³, C. van der Merwe³, C. L. van Dyk³², V. Van Tonder³, R. Van Wyk³, A. J. Venter³, M. Venter³, M. G. Welz³, L. P. Williams³, and B. Xiaia³

(Affiliations can be found after the references)

Received 7 June 2021 / Accepted 25 October 2021

ABSTRACT

MeerKAT's large number (64) of 13.5 m diameter antennas, spanning 8 km with a densely packed 1 km core, create a powerful instrument for wide-area surveys, with high sensitivity over a wide range of angular scales. The MeerKAT Galaxy Cluster Legacy Survey (MGCLS) is a programme of long-track MeerKAT *L*-band (900–1670 MHz) observations of 115 galaxy clusters, observed for ~6–10 h each in full polarisation. The first legacy product data release (DR1), made available with this paper, includes the MeerKAT visibilities, basic image cubes at ~8'' resolution, and enhanced spectral and polarisation image cubes at ~8'' and 15'' resolutions. Typical sensitivities for the full-resolution MGCLS image products range from ~3–5 $\mu\text{Jy beam}^{-1}$. The basic cubes are full-field and span $2^\circ \times 2^\circ$. The enhanced products consist of the inner $1.2^\circ \times 1.2^\circ$ field of view, corrected for the primary beam. The survey is fully sensitive to structures up to ~10' scales, and the wide bandwidth allows spectral and Faraday rotation mapping. Relatively narrow frequency channels (209 kHz) are also used to provide HI mapping in windows of $0 < z < 0.09$ and $0.19 < z < 0.48$. In this paper, we provide an overview of the survey and the DR1 products, including caveats for usage. We present some initial results from the survey, both for their intrinsic scientific value and to highlight the capabilities for further exploration with these data. These include a primary-beam-corrected compact source catalogue of ~626 000 sources for the full survey and an optical and infrared cross-matched catalogue for compact sources in the primary-beam-corrected areas of Abell 209 and Abell S295. We examine dust unbiased star-formation rates as a function of cluster-centric radius in Abell 209, extending out to $3.5 R_{200}$. We find no dependence of the star-formation rate on distance from the cluster centre, and we observe a small excess of the radio-to-100 μm flux ratio towards the centre of Abell 209 that may reflect a ram pressure enhancement in the denser environment. We detect diffuse cluster radio emission in 62 of the surveyed systems and present a catalogue of the 99 diffuse cluster emission structures, of which 56 are new. These include mini-halos, halos, relics, and other diffuse structures for which no suitable characterisation currently exists. We highlight some of the radio galaxies that challenge current paradigms, such as trident-shaped structures, jets that remain well collimated far beyond their bending radius, and filamentary features linked to radio galaxies that likely illuminate magnetic flux tubes in the intracluster medium. We also present early results from the HI analysis of four clusters, which show a wide variety of HI mass distributions that reflect both sensitivity and intrinsic cluster effects, and the serendipitous discovery of a group in the foreground of Abell 3365.

Key words. surveys – galaxies: clusters: general – radio continuum: general – catalogs – radio lines: general – galaxies: general

* Data are available at <https://doi.org/10.48479/7epd-w356>.

1. Introduction

Galaxy clusters are the largest gravitationally bound structures in the Universe and, as such, are powerful tools for a variety of research areas in both astrophysics and cosmology. Their composition is dominated by dark matter, with $\sim 13\%$ of their mass coming from the ionised plasma of the intracluster medium (ICM) and only $\sim 2\%$ from the stars of their constituent galaxies and cold gas. Some of these galaxies radiate at radio frequencies, either through star-formation processes or from nuclear activity in the galaxy's core (Condon 1992; Simpson et al. 2006; Luchsinger et al. 2015; Mancuso et al. 2017). Some radio galaxies with active galactic nuclei (AGN) exhibit large-scale radio jets or lobes (Fanaroff & Riley 1974), which can be disrupted by interaction with the ICM through merger-related or other processes (see e.g. Gunn & Gott 1972; Miley et al. 1972; Cowie & McKee 1975; Blanton et al. 2003).

Radio observations of clusters have also revealed steep-spectrum, diffuse radio emission (see reviews by Feretti et al. 2012; van Weeren et al. 2019), which can be used to study the distributed populations of cosmic ray particles and magnetic fields in the ICM, outside of individual radio or star-forming galaxies. These diffuse structures are closely linked to cluster mergers (Cassano et al. 2010; van Weeren et al. 2011a) and as such can also be used to study shock physics, merger-related turbulence, and other particle re-acceleration processes within the ICM (see reviews by Brunetti & Jones 2014; van Weeren et al. 2019, and references therein). Cluster observations carried out by wide-field instruments also contain many field sources, both along the cluster line of sight and in the surrounding area. These provide important information on the clusters themselves (e.g. by using background sources as Faraday rotation probes) and on radio galaxy physics outside of the dense cluster environments. Wide-field imaging enables both statistical studies, such as environment-sensitive properties of galaxy populations, and serendipitous studies of individual field sources (e.g. Brüggén et al. 2021).

MeerKAT¹ is a 64-dish radio interferometer that can observe the sky below a declination (Dec) of $+45^\circ$ (with an elevation limit of 15°), operating in the UHF (580–1015 MHz), *L* (900–1670 MHz), and *S* bands (1.75–3.5 GHz). Its specifications are described in detail in Jonas & MeerKAT Team (2016) and Camilo et al. (2018). MeerKAT's *L*-band system, with a primary beam full width at half maximum (FWHM) of 1.2° at 1.28 GHz, was the first to be commissioned, and in 2018 MeerKAT began a programme of long-track observations of galaxy clusters. This programme became the MeerKAT Galaxy Cluster Legacy Survey (MGCLS), using ~ 1000 h in the *L* band to observe 115 galaxy clusters in full polarisation between -80° and 0° Dec, spread out over the full range of right ascension (RA).

In addition to continuum and polarimetric studies, the deep, broadband, wide-field, sub- $10''$ resolution MGCLS observations provide a rich resource for studying neutral hydrogen in galaxies. Studies of HI morphologies in dense cluster environments and in the field, distributions of HI masses in different types of clusters, and the cosmic evolution of cluster HI out to redshifts of $z = 0.48$ are all enabled with these data, with a velocity resolution of ~ 44 km s⁻¹ at $z = 0$.

Here we present an overview of the MGCLS and the various legacy products being made available to the astronomical community. These data are a rich resource for many scientific

studies, both cluster-specific studies and those involving field sources. We provide some initial science findings in the areas of cluster diffuse emission, radio galaxy physics, star-forming systems, and neutral hydrogen mapping. In addition to their intrinsic value, these examples also demonstrate the potential of the legacy products for a wide range of astrophysical investigations.

The paper is organised as follows. In Sect. 2 we describe the target sample, with the observations and initial data processing described in Sect. 3. A discussion of the legacy data products, including caveats for use and some primary use cases, is provided in Sect. 4. Source catalogues are presented in Sect. 5. The next four sections present highlights of various science investigations that have been or can be carried out using the legacy products and visibilities: Sect. 6 focuses on cluster diffuse emission; Sect. 7 highlights some interesting individual radio sources; Sect. 8 presents results based on star-forming galaxies; and Sect. 9 highlights some HI science capabilities. A summary and concluding remarks are presented in Sect. 10. In this paper we assume a flat Λ cold dark matter cosmology with $H_0 = 70$ km s⁻¹ Mpc⁻¹, $\Omega_m = 0.3$, and $\Omega_\Lambda = 0.7$. We define the radio spectral index, α , such that $S_\nu \propto \nu^\alpha$, where S_ν is the flux density at frequency ν . In this paper R_{200} denotes the radius within which the average density is 200 times the critical density of the Universe. Unless otherwise noted, we give all synthesised beams in terms of FWHM values, and redshifts are taken from the NASA/IPAC right ascension (NED)² (Helou et al. 1991) or Vizier (Ochsenbein et al. 2000).

2. Cluster sample

The MGCLS sample consists of 115 galaxy clusters spanning a Dec range of -85 to 0° . The targeted clusters form a heterogeneous sample, with no mass or redshift selection criteria applied, and consist of two groups: 'radio-selected' and 'X-ray-selected'. The full list of MGCLS clusters is given in Table 1 where the listed RA and Dec are that of the MeerKAT pointing. The median redshift of the sample is 0.14, with only four clusters at $z > 0.4$.

2.1. Radio-selected sub-sample

The radio-selected sub-sample consists of 41 southern targets that have been previously searched for diffuse cluster radio emission by other studies. Targets were selected from published radio studies or reviews, namely Giovannini et al. (1999), Feretti et al. (2012), Lindner et al. (2014), Kale et al. (2015, 2017), Shakouri et al. (2016), Bonafede et al. (2017), George et al. (2017), Giacintucci et al. (2017), Parekh et al. (2017), and Golovich et al. (2019), and include both systems with and without previous diffuse emission detections. These previous radio studies were restricted to high-mass systems, $M_{500} \gtrsim 6 \times 10^{14} M_\odot$, derived from X-ray or Sunyaev-Zel'dovich effect (Sunyaev & Zeldovich 1972) data. Thus, the radio-selected sub-sample contains only high mass clusters. It covers a redshift range of $0.018 < z < 0.87$, with median $z = 0.22$.

Targeting systems of this nature ensured a high scientific return in terms of diffuse emission studies. However, due to the selection, this sub-sample is strongly biased towards clusters with radio halos and relics. The radio-selected clusters are listed

¹ Operated by the South African Radio Astronomy Observatory (SARAO).

² The NASA/IPAC Extragalactic Database is operated by the Jet Propulsion Laboratory, California Institute of Technology, under contract with the National Aeronautics and Space Administration.

Table 1. Observed cluster sample.

(1)	(2)	(3)	(4)	(5)	(6)	(7)	(8)	(9)	(10)	(11)
Cluster name	RA _{J2000} (deg)	Dec _{J2000} (deg)	<i>z</i>	Astrometry Fix	Posn	Pol.	rms (μ Jy beam ⁻¹)	DQF	D.E.	Alternate name
<i>Radio-selected sample</i>										
Abell 13	3.3842	-19.5010	0.094	-	✓	-	3.5	1	✓	MCXC J0013.6-1930
Abell 22	5.1608	-25.7220	0.142	✓	✓	✓	2.9	0	✓	MCXC J0020.7-2542
Abell 33	6.7792	-19.5067	0.280	-	✓	-	5.7	1	-	
Abell 85	10.4529	-9.3180	0.055	✓	✓	✓	3.3	1	✓	MCXC J0041.8-0918
Abell 133	15.6879	-21.8800	0.057	✓	✓	✓	6.7	1	-	MCXC J0102.7-2152
Abell 168	18.7908	0.2475	0.045	✓	✓	✓	3.6	2	✓	MCXC J0115.2+0019
Abell 194	21.4458	-1.3731	0.018	✓	✓	✓	5.7	1	-	MCXC J0125.6-0124
Abell 209	22.9896	-13.5764	0.206	✓	✓	✓	3.6	1	✓	MCXC J0131.8-1336
Abell 370	39.9604	-1.5856	0.375	✓	✓	-	6.9	2	✓	ZwCl 0237.2-0146
Abell 521	73.5358	-10.2442	0.253	-	✓	-	3.4	0	✓	MCXC J0454.1-1014
Abell 545	83.1017	-11.5431	0.154	✓	✓	-	3.1	1	✓	MCXC J0532.3-1131
Abell 548	86.7571	-25.6164	0.042	✓	✓	✓	2.8	1	-	
Abell 2485	342.1371	-16.1064	0.247	-	✓	-	2.8	0	-	MCXC J2248.5-1606
Abell 2597	351.3321	-12.1244	0.085	-	✓	-	6.0	2	-	MCXC J2325.3-1207
Abell 2645	355.3200	-9.0275	0.251	-	✓	-	4.3	2	✓	MCXC J2341.2-0901
Abell 2667	357.9196	-26.0836	0.230	-	✓	-	2.7	0	✓	MCXC J2351.6-2605
Abell 2744	3.5671	-30.3830	0.308	✓	✓	✓	2.9	0	✓	MCXC J0014.3-3023
Abell 2751	4.0580	-31.3885	0.107	✓	✓	✓	2.6	0	✓	MCXC J0016.3-3121
Abell 2811	10.5368	-28.5358	0.108	-	✓	-	2.6	0	✓	MCXC J0042.1-2832
Abell 2813	10.8517	-20.6214	0.292	-	✓	-	3.4	2	✓	MCXC J0043.4-2037
Abell 2895	19.5463	-26.9731	0.227	-	✓	-	3.0	1	✓	MCXC J0118.1-2658
Abell 3365	87.0500	-21.9350	0.093	-	✓	-	2.8	0	✓	
Abell 3376	90.4256	-39.9851	0.046	✓	✓	✓	3.1	1	✓	MCXC J0601.7-3959
Abell 3558	201.9783	-31.4922	0.048	✓	✓	-	2.9	1	✓	MCXC J1327.9-3130
Abell 3562	202.7833	-31.6731	0.049	✓	✓	✓	3.3	0	✓	MCXC J1333.6-3139
Abell 3667	303.1403	-56.8406	0.056	✓	✓	✓	4.2	1	✓	MCXC J2012.5-5649
Abell 4038	356.8796	-28.2028	0.028	✓	✓	✓	3.0	0	✓	MCXC J2347.7-2808
Abell S295	41.4000	-53.0380	0.300	✓	✓	✓	2.3	0	✓	PSZ1 G271.48-56.57
Abell S1063	342.1813	-44.5289	0.348	-	✓	-	2.6	0	✓	MCXC J2248.7-4431
Abell S1121	351.2844	-41.2118	0.190	-	✓	-	5.4	2	✓	PSZ2 G348.90-67.37
Bullet ^(†)	104.6579	-55.9500	0.296	✓	✓	-	2.8	0	✓	MCXC J0658.5-5556
El Gordo	15.7188	-49.2495	0.870	✓	✓	-	1.5	0	✓	ACT-CL J0102-4915
MACS J0025.4-1222	6.3724	-12.3770	0.584	✓	✓	-	3.7	1	-	MCXC J0025.4-1222
MACS J0257.6-2209	44.4179	-22.1628	0.322	-	✓	-	3.2	1	✓	MCXC J0257.6-2209
MACS J0417.5-1155	64.3942	-11.9089	0.440	✓	✓	-	2.9	0	✓	MCXC J0417.5-1154
PLCK G200.9-28.2	72.5871	-2.9493	0.220	✓	✓	✓	4.4	1	✓	
RXC J0225.1-2928	36.3750	-29.5000	0.060	✓	✓	-	5.1	2	-	MCXC J0225.1-2928
RXC J0510.7-0801	77.6846	-8.0200	0.220	✓	✓	-	5.2	1	✓	MCXC J0510.7-0801
RXC J0520.7-1328	80.1967	-13.5022	0.336	✓	✓	-	7.7	2	✓	PSZ1 G215.29-26.09
RXC J1314.4-2515	198.5988	-25.2558	0.249	✓	✓	-	4.2	1	✓	MCXC J1314.4-2515
RXC J2351.0-1954	357.7704	-19.9133	0.248	-	✓	-	3.1	1	✓	
<i>X-ray-selected sample</i>										
J0014.3-6604	3.5767	-66.0775	0.155	✓	✓	-	2.5	0	-	Abell 2746
J0027.3-5015	6.8388	-50.2511	0.145	✓	✓	-	2.6	0	✓	Abell 2777
J0051.1-4833	12.7967	-48.5597	0.187	✓	✓	-	2.6	0	-	Abell 2830
J0108.5-4020	17.1383	-40.3500	0.143	✓	✓	-	2.6	0	-	Abell 2874
J0117.8-5455	19.4604	-54.9239	0.251	✓	✓	-	2.4	0	-	RXC J0117.8-5455
J0145.0-5300	26.2596	-53.0139	0.118	✓	✓	-	2.6	1	✓	Abell 2941

Notes. Columns: (1) Cluster name, listed alphabetically: Radio-selected targets are indicated by their common name (top panel), X-ray-selected targets are indicated by their MCXC catalogue designation (bottom panel). See Sect. 2 for details; (2) and (3) MeerKAT pointing coordinates: J2000 RA and Dec; (4) Cluster redshift; (5)–(7) Product status: Astrometry (see Sect. 4.4.4) – corrected mapping (Fix) and positional offsets (Posn); Polarisation mapped (Pol.); (8) Image sigma-clipped standard deviation; (9) Data quality flag: 0 – Good dynamic range, 1 – Moderate dynamic range with some artefacts around bright sources, 2 – Poor dynamic range with high contamination by bright source artefacts, 3 – Poor dynamic range with ripples across image; (10) Presence of diffuse cluster emission; see Table 4 for more details; (11) Alternate cluster name. ^(†) Observed as part of the X-ray-selected sample; data products can be found under the MCXC designation, J0658.5-5556.

Table 1. continued.

(1) Cluster name	(2) RA _{J2000} (deg)	(3) Dec _{J2000} (deg)	(4) <i>z</i>	(5) Astrometry Fix	(6) Posn	(7) Pol.	(8) rms (μ Jy beam ⁻¹)	(9) DQF	(10) D.E.	(11) Alternate name
J0145.2–6033	26.3196	−60.5650	0.184	✓	✓	–	2.3	0	✓	PSZ1 G291.34–55.32
J0212.8–4707	33.2246	−47.1328	0.115	✓	✓	–	3.1	1	–	Abell 2988
J0216.3–4816	34.0796	−48.2731	0.163	✓	✓	✓	3.1	3	✓	Abell 2998
J0217.2–5244	34.3025	−52.7469	0.343	✓	✓	–	2.8	1	✓	ACT-CL J0217–5245
J0225.9–4154	36.4775	−41.9097	0.220	✓	✓	–	2.7	1	✓	Abell 3017
J0232.2–4420	38.0700	−44.3475	0.284	✓	✓	✓	2.6	0	✓	PSZ2 G259.98–63.43
J0303.7–7752	45.9433	−77.8692	0.274	✓	✓	–	2.9	0	✓	PSZ1 G294.68–37.01
J0314.3–4525	48.5825	−45.4242	0.073	✓	✓	✓	2.5	0	✓	Abell 3104
J0317.9–4414	49.4938	−44.2389	0.075	✓	✓	–	3.0	2	–	Abell 3112
J0328.6–5542	52.1563	−55.7128	0.086	✓	✓	✓	2.9	1	–	Abell 3126
J0336.3–4037	54.0779	−40.6222	0.062	✓	✓	–	3.5	1	–	Abell 3140
J0342.8–5338	55.7246	−53.6353	0.060	✓	✓	–	3.4	0	✓	Abell 3158
J0351.1–8212	57.7871	−82.2167	0.061	✓	✓	✓	2.8	0	✓	Abell S405
J0352.4–7401	58.1229	−74.0308	0.127	✓	✓	✓	2.6	0	✓	Abell 3186
J0406.7–7116	61.6908	−71.2750	0.229	✓	✓	–	3.0	1	–	
J0416.7–5525	64.1871	−55.4189	0.365	✓	✓	–	2.7	0	–	
J0431.4–6126	67.8504	−61.4439	0.059	✓	✓	✓	4.5	1	✓	Abell 3266
J0449.9–4440	72.4800	−44.6781	0.172	✓	✓	–	2.6	0	–	Abell 3292
J0510.2–4519	77.5575	−45.3211	0.200	✓	✓	–	3.0	0	✓	Abell 3322
J0516.6–5430	79.1583	−54.5142	0.297	✓	✓	✓	3.1	1	✓	Abell S520
J0525.8–4715	81.4650	−47.2506	0.191	✓	✓	–	3.0	1	–	Abell 3343
J0528.9–3927	82.2346	−39.4628	0.284	✓	✓	–	2.6	0	✓	PSZ2 G244.37–32.15
J0540.1–4050	85.0263	−40.8422	0.036	✓	✓	–	4.1	1	–	Abell S540
J0540.1–4322	85.0417	−43.3822	0.085	✓	✓	✓	3.4	1	–	Abell 3360
J0542.8–4100	85.7117	−41.0014	0.640	✓	✓	–	2.4	0	–	CL J0542.8–4100
J0543.4–4430	85.8517	−44.5053	0.164	✓	✓	–	3.6	1	–	
J0545.5–4756	86.3775	−47.9406	0.130	✓	✓	–	2.9	1	–	Abell 3363
J0600.8–5835	90.2013	−58.5872	0.037	✓	✓	–	2.5	0	–	Abell S560
J0607.0–4928	91.7558	−49.4833	0.056	✓	✓	✓	2.8	1	–	Abell 3380
J0610.5–4848	92.6333	−48.8072	0.243	✓	✓	–	2.8	0	–	
J0616.8–4748	94.2233	−47.8050	0.116	✓	✓	–	3.0	0	–	PSZ1 G255.64–25.30
J0625.2–5521	96.3179	−55.3517	0.121	✓	✓	–	5.3	1	–	
J0626.3–5341	96.5950	−53.6956	0.051	✓	✓	–	4.4	2	–	Abell 3391
J0627.2–5428	96.8100	−54.4700	0.051	✓	✓	✓	7.8	2	✓	Abell 3395
J0631.3–5610	97.8363	−56.1722	0.054	✓	✓	–	2.7	0	✓	
J0637.3–4828	99.3288	−48.4783	0.203	✓	✓	✓	3.0	0	✓	Abell 3399
J0638.7–5358	99.6938	−53.9717	0.233	✓	✓	✓	3.4	1	✓	Abell S592
J0645.4–5413	101.3721	−54.2189	0.167	✓	✓	–	3.4	1	✓	Abell 3404
J0658.5–5556 ^(†)	104.6296	−55.9469	0.296	✓	✓	–	3.2	0	✓	Bullet
J0712.0–6030	108.0225	−60.5017	0.032	✓	✓	–	2.7	1	–	
J0738.1–7506	114.5375	−75.1067	0.111	✓	✓	–	2.6	0	–	PSZ1 G287.05–23.21
J0745.1–5404	116.2900	−54.0789	0.074	✓	✓	✓	3.1	0	✓	CIZA J0745.1–5404
J0757.7–5315	119.4438	−53.2636	0.043	✓	✓	–	3.2	0	–	Abell S606
J0812.5–5714	123.1263	−57.2350	0.062	✓	✓	✓	2.9	0	–	PSZ2 G271.60–12.50
J0820.9–5704	125.2483	−57.0797	0.061	✓	✓	✓	2.9	2	✓	PSZ1 G272.08–11.51
J0943.4–7619	145.8542	−76.3325	0.199	✓	✓	–	4.4	2	–	CIZA J0943.4–7619
J0948.6–8327	147.1642	−83.4656	0.198	✓	✓	✓	3.1	0	–	
J1040.7–7047	160.1867	−70.7969	0.061	✓	✓	✓	4.3	1	–	CIZA J1040.7–7047
J1130.0–4213	172.5233	−42.2297	0.155	✓	✓	–	2.9	1	✓	PSZ1 G287.22+18.13
J1145.6–5420	176.4108	−54.3414	0.155	✓	✓	–	3.1	1	–	PSZ1 G293.32+07.33
J1201.0–4623	180.2642	−46.3906	0.118	✓	✓	–	3.2	0	–	CIZA J1201.0–4623
J1240.2–4825	190.0571	−48.4328	0.152	✓	✓	–	3.3	1	–	
J1248.7–4118	192.1996	−41.3078	0.011	✓	✓	–	7.1	2	–	Abell 3526
J1358.9–4750	209.7371	−47.8386	0.074	✓	✓	✓	3.6	1	–	CIZA J1358.9–4750
J1410.4–4246	212.6188	−42.7769	0.049	✓	✓	–	3.6	1	–	CIZA J1410.4–4246

Table 1. continued.

(1)	(2)	(3)	(4)	(5)	(6)	(7)	(8)	(9)	(10)	(11)
Cluster name	RA _{J2000} (deg)	Dec _{J2000} (deg)	z	Astrometry Fix	Posn	Pol.	rms ($\mu\text{Jy beam}^{-1}$)	DQF	D.E.	Alternate name
J1423.7–5412	215.9304	−54.2033	0.300	✓	✓	–	3.5	1	✓	CIZA J1423.7–5412
J1518.3–4632	229.5950	−46.5403	0.056	✓	✓	✓	5.5	1	–	CIZA J1518.3–4632
J1535.1–4658	233.7879	−46.9792	0.036	✓	✓	–	4.4	3	–	CIZA J1535.1–4658
J1539.5–8335	234.8913	−83.5922	0.073	✓	✓	✓	2.7	0	✓	
J1601.7–7544	240.4446	−75.7461	0.153	✓	✓	✓	3.7	1	✓	PSZ2 G313.88–17.11
J1645.4–7334	251.3592	−73.5817	0.069	✓	✓	✓	4.8	2	–	PSZ2 G317.58–17.82
J1653.0–5943	253.2533	−59.7331	0.048	✓	✓	✓	3.6	3	–	PSZ1 G329.36–09.88
J1705.1–8210	256.2929	−82.1739	0.074	✓	✓	✓	2.8	0	–	Abell S792
J1840.6–7709	280.1550	−77.1556	0.019	✓	✓	–	19.0	1	✓	
J2023.4–5535	305.8500	−55.5917	0.232	✓	✓	✓	2.7	1	✓	PSZ1 G342.33–34.92
J2104.9–8243	316.2446	−82.7228	0.097	✓	✓	✓	2.6	0	–	Abell 3728
J2222.2–5235	335.5579	−52.5869	0.174	✓	✓	–	4.0	1	–	Abell 3870
J2319.2–6750	349.8000	−67.8400	0.029	✓	✓	✓	3.5	1	–	Abell 3990
J2340.1–8510	355.0429	−85.1783	0.193	✓	✓	✓	3.0	1	–	Abell 4023

in the first panel of Table 1, using their common names. Where available, an alternate name is provided in the final column of the table. In cases where multiple alternate names exist, the Meta-Catalogue of X-ray-detected Clusters (MCXC; Piffaretti et al. 2011) designation, if available, is given.

2.2. X-ray-selected sub-sample

The X-ray-selected sub-sample, making up 64% of the MGCLS, was selected from the MCXC catalogue, in order to create a sample with no direct prior biases towards or against cluster radio properties. From the list of clusters in the MCXC catalogue that were south of -39° , we selected MGCLS targets as needed to fill gaps in MeerKAT’s observing schedule.

The X-ray-selected clusters, which cover a redshift range of $0.011 < z < 0.640$ with a median of $z = 0.13$, are listed in the second panel of Table 1 using their MCXC catalogue designations. Where relevant, common alternate names are also listed. The X-ray-selected sample covers a luminosity range of $L_X \sim (0.1-30) \times 10^{44} \text{ erg s}^{-1}$, with $\sim 60\%$ of clusters in the range $10^{44}-10^{45} \text{ erg s}^{-1}$.

3. Observations and data reduction

3.1. Observations

The MGCLS observations were carried out between June 24, 2018, and June 16, 2019, using the full MeerKAT array, with a minimum of 59 antennas per observation. The MGCLS clusters were observed using MeerKAT’s L-band receiver (with nominal radio frequency band of 900–1670 MHz) in the 4k correlator mode (4096 channels across the digitised band of 856–1712 MHz) with 8 s integrations.

Data consists of all combinations of the two orthogonal linearly polarised feeds. Each dataset contains observations of the flux density, delay, and bandpass calibrators PKS B1934–638 and/or PMN J0408–6545. These were observed for 10 min every hour with the remaining time cycling between the target cluster (10 min) and a nearby astrometric and phase calibrator (1 min). These observations spanned 8–12 h, cycling between the target cluster and the various calibrator sources, and typically consisted of $\sim 5.5-9.5$ h on source integration, sometimes divided

into multiple sessions. These were scheduled as ‘fillers’ during observing schedule gaps.

3.2. Initial processing

All datasets were calibrated and imaged with a simple procedure, described in Mauch et al. (2020), which also verified the data quality. All calibration and imaging used the OBIT package³ (Cotton 2008).

3.2.1. Calibration and editing

Various processes as described in Mauch et al. (2020) were used to identify data affected by interference and/or equipment failures, which were then edited out, typically resulting in $\sim 50\%$ of the frequency and/or time samples being removed. The remaining data were calibrated in group delay, bandpass, and amplitude and phase. The reference antenna was picked on the basis of the best signal-to-noise ratio (S/N) in the bandpass solutions. Our flux density scale is based on the spectrum of PKS B1934–638 (Reynolds 1994):

$$\log(S) = -30.7667 + 26.4908 \log(\nu) - 7.0977 \log(\nu)^2 + 0.6053 \log(\nu)^3, \quad (1)$$

where S is the flux density in Jy and ν is the frequency in MHz. The uncertainty in the flux-density scale is estimated to be $\sim 5\%$.

Small errors in both time and frequency tagging were discovered after the observations had started and were subsequently corrected. These errors have a small effect on the images, and are more fully described in Sect. 4.4.4. The majority of images were made after the errors were fixed.

3.2.2. Stokes-I imaging

We created the maps using the OBIT wide-band, wide-field imager MFImage. MFImage uses facets to correct for the curvature of the sky, and multiple frequency bins, which are imaged independently and deconvolved jointly, to allow for the antenna

³ <http://www.cv.nrao.edu/~bcotton/Obit.html>

gains and a sky brightness distribution that vary with frequency. A frequency-dependent taper was used to obtain a resolution that remained approximately constant over our $\sim 2:1$ range in frequency. MFImage is described in more detail in Cotton et al. (2018).

The sky within a radius of 0.8° to 1° of the pointing centre was fully imaged, with outlying facets added to cover sources from the Sydney University Molonglo Sky Survey (SUMSS; Bock et al. 1999) 843 MHz catalogue (Mauch et al. 2003) brighter than 5 mJy within 1.5° . Two iterations of phase-only self-calibration, with a 30 s solution interval, were used. Amplitude and phase self-calibration were added if the image contained a pixel with a brightness in excess of 0.3 Jy beam^{-1} . For Stokes- I imaging we used a maximum of 30 000 components, a loop gain of 0.1, and fields were typically CLEANed to a depth of $\sim 50 \mu\text{Jy beam}^{-1}$. No direction-dependent corrections were applied; such corrections may be useful for followup studies of individual fields, but do not affect the science results presented here.

Robust weighting (-1.5 in AIPS/OBIT usage) was used to down-weight the very densely sampled inner portion of the uv -plane. The resulting FWHM resolution was in the range $7.5\text{--}8.0''$. We made images consisting of 14 frequency bins, each with a 5% fractional ($\Delta\nu/\nu$) bandpass. When the imaging was complete, a spectrum was fitted in each pixel of the resulting cube. Off-source noise levels (rms) in images that were not dynamic range limited ranged over $\sim 3\text{--}5 \mu\text{Jy beam}^{-1}$. This is close to the expected thermal noise, with rms confusion expected to be of the order of $1 \mu\text{Jy beam}^{-1}$ (Mauch et al. 2020). The local rms noise varies over the field of view due to contributions from (multiple) strong sources and is a strong function of the target pointing. Primary beam corrections were only applied to the ‘enhanced products’ (see Sect. 4.2).

3.2.3. Reprocessing with polarimetry

Changes from the standard procedure described in Sect. 3.2.1 were needed for polarisation calibration. The MGCLS observations did not contain observations of a polarised calibrator to calibrate the polarisation response of the array. However, each MeerKAT observing session is begun with a calibration using noise signals injected into each antenna that can be used to calibrate the bulk of the phase and delay difference between the two recorded orthogonal linear polarisations. The remainder of the signal path is stable enough that, after this initial calibration, appropriate polarisation calibration is possible using calibration parameters derived from other, properly polarisation-calibrated, data. This procedure is discussed in detail in Plavin et al. (2020); however, we outline the basic steps here for clarity.

Prior to any calibration derived from the data, the initial calibration of the ‘X’ and ‘Y’ linear feeds from the injected noise signals was performed; this removes most of the phase and delay difference between the X and Y systems. The remainder is sufficiently stable that a ‘standard’ calibration using the same reference antenna corrects it. In the parallel hand calibration the two bandpass calibrators, PKS B1934–638 and PMN J0408–6545, are sufficiently weakly polarised that they can be considered unpolarised. After bandpass calibration subsequent gain calibration solved only for Stokes- I terms to avoid disturbing the relative X/Y gain ratio.

Following the parallel-hand calibration, our polarisation calibration procedure was as follows. We required the selected calibration reference antenna to have a set of averaged polarisation calibrations derived from other MeerKAT datasets that had ade-

quate polarisation calibration (including a polarised calibrator). This ‘standard’ set of calibration tables was used to complete the X–Y phase calibration and to correct for on-axis instrumental polarisation via the feed ellipticity and orientation⁴. Since the antennas are equipped with linear feeds, the fundamental reference for the polarisation angle is the nominal orientation of the feeds.

The standard polarisation calibration source 3C286 was used to verify and make final corrections to the polarisation calibration. This source has a polarisation angle of -33° and a rotation measure (RM) equal to zero (Perley & Butler 2013). A correction of several degrees in polarisation angle and about 1 rad m^{-2} in RM is needed to reproduce the assumed polarisation. These corrections are stable over several years and have been applied to all polarisation corrected data.

A selected subset of the clusters were re-calibrated and imaged in MFImage to produce Stokes I , Q , U , and V images; these clusters are indicated in the ‘Poln’ column in Table 1. Due to the lack of internal polarisation calibration, the Stokes V images are not sufficient to detect weakly circular polarised sources, but can work as an overall check of the quality of the calibration. Strongly circularly or linearly polarised sources ($>1\%$) should be easily detectable.

3.2.4. Polarisation imaging

The imaging in full polarisation was similar to the initial imaging in Stokes I (Sect. 3.2.2), but wider and deeper. We used the same 5% frequency bins and the total bandwidth used by the Stokes- I imaging, which allows the recovery of RMs up to $\pm 100 \text{ rad m}^{-2}$ at full sensitivity, with decreasing sensitivity beyond this range. The field of view fully imaged has a radius of 1.2° . In Stokes I , we cleaned to a depth of $\sim 80 \mu\text{Jy beam}^{-1}$, using up to 500 000 components. Stokes Q and U were CLEANed to a depth of $\sim 30 \mu\text{Jy beam}^{-1}$ with up to 50 000 components. Off-source noise values in images that were not dynamic range limited were $\sim 3 \mu\text{Jy beam}^{-1}$.

4. MGCLS data products

The first MGCLS data release (DR1) is made public with this paper⁵, which consists of the MGCLS visibilities, the basic data products (described in Sect. 4.1), and a set of enhanced products (described in Sect. 4.2). All DR1 legacy products are available through a DOI⁶, and the raw visibilities are accessible through the South African Radio Astronomy Observatory (SARAO) Archive Server⁷ with project ID ‘SSV–20180624–FC–01’. We highlight the primary capabilities of the MGCLS data products in Sect. 4.3. (For issues relating to the scientific usability of the various products, see Sect. 4.4).

4.1. Basic products

The basic MGCLS product consists of the standard MFImage output, the structure and description of which are given in Cotton (2019). The basic image product is a cube consisting of 16

⁴ These standard sets of calibration tables are not part of the MGCLS but can be provided upon reasonable request.

⁵ When using DR1 products, this paper should be cited, and the MeerKAT telescope acknowledgement included. See <https://doi.org/10.48479/7epd-w356> for details.

⁶ <https://doi.org/10.48479/7epd-w356>

⁷ <https://archive.sarao.ac.za/>

planes: (1) the brightness at the reference frequency (typically 1.28 GHz, although there are slight variations depending on the observation), from a pixel-by-pixel least-squares fit to the brightness, I , in each frequency channel; (2) the spectral index, α_{908}^{1656} , from the above fit, or a default value of -0.6 , as described below; and (3)–(16) images in frequency channels centred at 908, 952, 996, 1044, 1093, 1145, 1200, 1258, 1318, 1382, 1448, 1482, 1594, and 1656 MHz; the 1200 and 1258 MHz channels are totally blanked for radio frequency interference (RFI).

It should be noted that none of these have primary beam corrections, thus the brightness values and spectral index estimates are biased by the frequency-variable primary beam shape, and are not suitable for quantitative scientific use. These basic products are useful, however, for full-field visual searches and source-finding. Images in Stokes Q , U , and V are provided where available.

4.2. Enhanced products

4.2.1. Primary-beam-corrected image and spectral index cubes

The basic images were corrected for the primary beam at each frequency, as described in [Mauch et al. \(2020\)](#), both at the full resolution of the image, typically $7.5\text{--}8''$, and at a convolved $15''$ resolution to help recover low-surface-brightness features. The primary-beam-corrected images show the inner $1.2^\circ \times 1.2^\circ$ portion of the MGCLS pointing, as primary beam corrections are unreliable beyond this region. Stokes Q , U , and V cubes are provided where available.

The final enhanced image data products are five-plane cubes (referred to as the *5pln* cubes in the following) in which the first plane is the brightness at the reference frequency, and the second is the spectral index, α_{908}^{1656} , both determined by a least-squares fit to $\log(I)$ versus $\log(\nu)$ at each pixel. The third plane is the brightness uncertainty estimate, fourth is the spectral index uncertainty, and fifth is the χ^2 of the least-squares fit. Uncertainty estimates are only the statistical noise component and do not include calibration or other systematic effects. As described in more detail below (see Sect. 4.4.2), a default value of -0.6 is given for the spectral index when the S/N is too low for an accurate fit.

4.2.2. Primary-beam-corrected frequency cubes

We also provide primary-beam-corrected frequency cubes at full and $15''$ resolutions. These cubes consist of the 12 non-blanked frequency planes with centre frequencies as listed in Sect. 4.1. To account for the unreliability of primary beam corrections far from the pointing centre, pixels are blanked as for the *5pln* cubes discussed above. Stokes Q , U , and V cubes are provided when available.

4.3. Primary use cases

The MGCLS legacy products described in Sect. 4 provide powerful datasets for a range of scientific inquiry. Here we highlight the main use cases for the MGCLS data.

4.3.1. Sensitivity to a range of scales

The configuration of the MeerKAT array, with its dense 1 km diameter core of antennas and maximum 7.7 km baseline, allows for exceptional instantaneous sensitivity to a wide range of angular scales. The full-resolution maps have synthesised beam sizes

of $\sim 7.5\text{--}8''$ and rms image noise levels of $\sim 3\text{--}5 \mu\text{Jy beam}^{-1}$, and are sensitive to extended structures up to tens of arcminutes in extent. An example of the central region of one of the MGCLS fields, MCXC J0027.3–5015, is shown in panel A of Fig. 1. The left figure of panel A shows the full-resolution ($7.4'' \times 7.0''$) image, dominated by compact sources with faint extended structure at the centre. To increase the sensitivity to the larger scale structure, the typical procedure is to convolve to a lower resolution. The middle figure shows the convolved $25''$ resolution map of the same patch of sky, which is badly ‘confused’ due to blending of the compact sources, masking the underlying diffuse emission.

To exploit MeerKAT’s sensitivity to large-scale structures, without the problem of source confusion, we filter out all small-scale structure with the technique of [Rudnick \(2002\)](#) using a box size of 19 pixels ($23.75''$), and convolve the resulting ‘diffuse emission’ image to $25''$. Using Fig. 3 in that paper, we can roughly quantify what percentage of the flux will be in the diffuse emission image as a function of the characteristic size of any structure. For a $60''$ structure, $\sim 82\%$ of the flux will be included, with higher percentages for structures of increasing sizes. Smaller scale features will be heavily suppressed, with only 5–10% of the flux remaining at $15''$, and $\sim 0\%$ at $8''$. The result of this process is shown in the right figure of panel A in Fig. 1, where the structure of the diffuse emission is readily visible. The filtered $25''$ resolution or diffuse emission maps referred to in the following sections are made using the above filtering technique. We note that these filtered maps are not included in the legacy products.

4.3.2. In-band spectral index maps

MeerKAT’s wide 0.8 GHz bandwidth in the L band allows for in-band spectral index studies, with primary-beam-corrected spectral index and associated uncertainty maps being part of the legacy products. Panel B of Fig. 1 shows an example spectral index map for a MGCLS radio galaxy with diffuse lobes. As per the caveats discussed in Sect. 4.4.2, a reliable spectral index can only be fit for pixels with $S/N \gtrsim 10$. Spectral index uncertainty maps contain only the statistical uncertainty from the fit, with constrained spectral indices typically having per-pixel statistical uncertainties between 0.05 and 0.2.

4.3.3. Polarisation studies

All of the MGCLS targets were observed in full polarisation, with 44 of the clusters being mapped in polarisation for DR1 (see Table 1 at the end of the paper for the full list). Allowing for the caveats mentioned in Sect. 4.4.5, the sensitivity of the MGCLS polarisation maps will allow for the detection and determination of RMs for a large population of radio sources. Such detections will allow statistical studies of cluster magnetic fields. The determination of RMs of extended sources at high spatial sensitivity will also allow a detailed study of magnetic field strengths and structure across various source morphologies (e.g. radio galaxies and relics). Panel C of Fig. 1 shows an RM map for one such extended source in the Abell 3667 field. This map is discussed in more detail in Sect. 6.1.3.

4.3.4. H I capabilities

In addition to the continuum and polarimetric use cases, the MGCLS visibilities can also be used for H I studies. The MGCLS frequency resolution of 209 kHz corresponds to an H I